Magnetic Field of Light Unlocks Topological Entanglement in Solids - Supplemental Material

Victor Kärcher[1,2], Tobias Reiker[1], and Helmut Zacharias[1]

[1] *Center for Soft Nanoscience, University of Münster, 48149 Münster, Germany*
[2] *Department of Physics, University of Münster, 48149 Münster, Germany*

October 28, 2025

Contents

1 Experimental Set-up

Fig. S1 shows the experimental setup used in this study. We employ an Yb-doped fiber laser system (Active Fiber Systems) with a central wavelength of $\lambda_0 = 1030\,\text{nm}$, corresponding to a central frequency of $\omega_0 = 2\pi \cdot 291\,\text{THz}$, and a pulse duration of $\tau \approx 40\,\text{fs}$. The pulses propagate through a $2f$ system with focal lengths of $f = 150\,\text{mm}$. The quartz crystal is placed approximately 1.5 mm beyond the focus to prevent damage. After the $2f$ system, the fundamental and generated harmonics pass through a CaF_2 prism pair to separate the harmonics from the fundamental. The fundamental is directed to a beam dump, while the harmonic spectra are recorded using a commercial Avantes spectrometer. Sample rotation is controlled by a custom-built motorized stage, operated via a self-written MATLAB program.

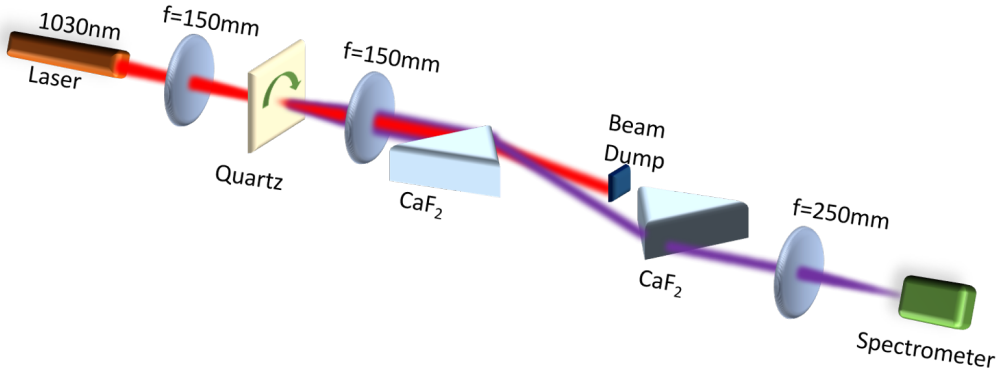

Figure S1: Experimental set-up used for this study.

2 Electronic structure of Quartz

In its ideal form, quartz possesses a wide band gap of $E_g = 8.9\,\text{eV}$, with the HOMO-LUMO splitting illustrated in Fig. S2. However, defect centers in real crystals introduce intermediate states within the band gap. A negatively charged vacancy center exhibits distinct optical and magnetic properties through its interactions with neighboring atoms. Optical absorption

bands arise at approximately 3.7 eV, with a bandwidth of about $\Delta E = 0.3\,\mathrm{eV}$ at 1σ ($\Gamma \approx 2\pi \times 70\,\mathrm{THz}$), and another band near 4.6 eV [1]. The latter corresponds to a transition from a doubly occupied σ-type bonding state (located at the top of the valence band) to a singly occupied σ^*-state (manifested as split left and right lines at the bottom of the conduction band). The first transition, critical for this study, corresponds to the excitation from the singly occupied σ^*-state to the lowest conduction band and is strongly influenced by the Si–Si distance [2].

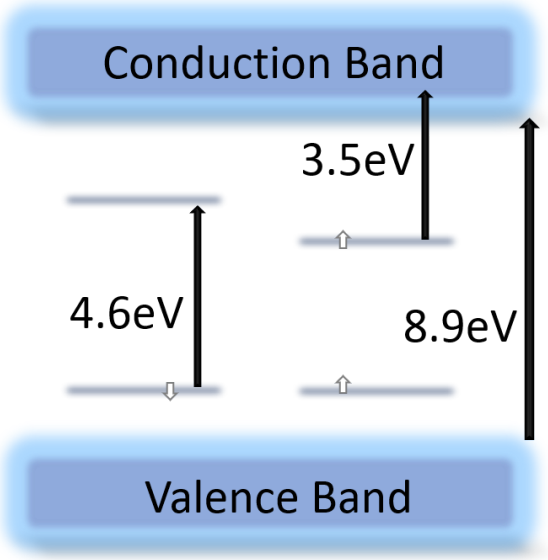

Figure S2: Schematic representation of the electronic structure of quartz with an overall bandgap of $E_g = 8.9\,\mathrm{eV}$. The oxygen vacancy induces two localized intermediate states with broadband absorption bands around 3.5 eV [2] or 3.7 [1] eV and around 4.6 eV.

3 Electrons in a Periodic Potential

In this section we will briefly describe the motion of electrons in a periodic crystal lattice[3]. We assume, that the reader knows exactly where the operator notation is needed and thus, we omit the operator notation (e.g. $H = \hat{H}$)

Let's consider the Hamiltonian for N_e electrons

$$H = \sum_{i=1}^{N_e} \frac{p_i^2}{2m_e} + U(\vec{r}_i), \tag{S1}$$

where p_i is the momentum operator of the i^{th} electron, m_e is the electrons mass and $U(\vec{r}) = U(\vec{r} + \vec{R}_j)$ is the periodic crystal potential with lattice vectors $\vec{R}_j$. The energy $\mathcal{E}_i$ of the i^{th} electron can be obtained by solving the Schrödinger Equation (SE)

$$H_i\psi_i(\vec{r}_i) = \mathcal{E}_i\psi_i(\vec{r}_i) \iff \left[-\frac{\hbar^2}{2m_e}\nabla_i^2 + U(\vec{r}_i)\right] = \mathcal{E}_i\psi_i(\vec{r}_i), \tag{S2}$$

where $\hbar$ is the Planck constant. We can now ignore the index i. By using the Bloch condition

$$\psi(\vec{r} + \vec{R}) = \exp(i\vec{k}\vec{R})\psi(\vec{r}) \tag{S3}$$

we can define periodic functions in the reciprocal space as

$$u_k(\vec{r}) = \exp(-i\vec{k}\vec{r})\psi_k(\vec{r}) \tag{S4}$$

and thus the wave functions are written as

$$\psi_k(\vec{r}) = \frac{1}{\sqrt{V_E}} \exp(i\vec{k}\vec{r})u_k(\vec{r}), \tag{S5}$$

where V_E is the volume of the elementary unit cell. eq. (S5) is known as the Bloch-Theorem and $u_k(\vec{r})$ is the Bloch-Factor. Hence, the energy dispersion $\mathcal{E}(\vec{k})$ can be calculated for all $\vec{k}-$points in the first Brillouin-Zone (BZ) by solving the following Schrödinger equation

$$\left[\frac{\hbar^2}{2m_e}\left(\frac{1}{i}\nabla + \vec{k}\right)^2 + U(\vec{r})\right] u_k(\vec{r}) = \mathcal{E}(\vec{k})u_k(\vec{r}). \tag{S6}$$

For all $\vec{k}-$points the Kramer's-Theorem[4]

$$\mathcal{E}_n(\vec{k}) = \mathcal{E}_n(-\vec{k}) \tag{S7}$$

is valid, where n denotes the valence band or the conduction band.

4 Electron Motion in Solids - External Electric Field

Here we present a brief and straight forward calculation for an electron accelerated in an external electric field in a wide bandgap solid. Starting from the acceleration theorem [5], the electrons velocity $\vec{v}(\vec{k})$ in a solid moving with momentum $\vec{k}$ can be obtained from

$$\vec{v}(\vec{k}) = \frac{1}{\hbar}\frac{\partial \mathcal{E}(\vec{k})}{\partial \vec{k}}. \tag{S8}$$

The electrons momentum accelerated in an electromagnetic field can be gained by integrating the equation of motion

$$m^*\ddot{\vec{r}} = -e\left(\vec{E} + \dot{\vec{r}} \times \vec{B}\right), \tag{S9}$$

where $m^* = \hbar^2 \left(\frac{\partial^2 \mathcal{E}(\vec{k})}{\partial \vec{k}^2}\right)^{-1}$ is the effective mass of the electron, e the elementary charge, $\vec{E}$ is the external electric field, and $\vec{B}$ is the magnetic field. Assuming the electric field $\vec{E}(t) = E_0 \cos(\omega_0 t)\vec{e}_x$ is polarized in x-direction, the time-dependent velocity $\dot{x}_\parallel$ and the location $x_\parallel$ are then given by

$$\begin{aligned} m^*\ddot{x}_\parallel &= -eE_0 \cos(\omega_0 t) \\ \iff \dot{x}_\parallel &= -\frac{eE_0}{m^*\omega_0}\sin(\omega_0 t) \\ \iff x_\parallel &= \frac{eE_0}{m^*\omega_0^2}\cos(\omega_0 t). \end{aligned} \tag{S10}$$

The momentum in x-direction parallel to the electric field is then given by

$$k_\parallel = \frac{m^*\dot{x}_\parallel}{\hbar} = -\frac{eE_0}{\hbar\omega_0}\sin(\omega_0 t). \tag{S11}$$

The band dispersion can always be expanded in terms of Fourier coefficients and by following the Kramers Theorem [4] after eq. (S7)

$$\mathcal{E}(\vec{k}) = \sum_{\tilde{n}=1}^{\tilde{n}_{\max}} \tilde{A}_n \cos\left(\sum_i \tilde{n} k_i a_i\right) \overset{\tilde{n}_{max}=1}{=} \tilde{A} \cos\left(\sum_i k_i a_i\right), \tag{S12}$$

where $\tilde{A}_{\tilde{n}}, \tilde{A}$ are the Fourier amplitudes and a_i the lattice constant in direction i where $i = \{x, y, z\}$. $\tilde{n}$ denotes the number of neighbouring atoms and for our case we use $\tilde{n} = 1$. Using eq. (S8), (S11) and (S12) we now can calculate the parallel velocity of the electron in the solid

$$v^{\parallel}(k_{\parallel}) = -\tilde{A}\frac{a}{\hbar} \sin\left(-\frac{eE_0 a}{\hbar\omega_0} \sin(\omega_0 t)\right) \tag{S13}$$

We can use the Jacobi-Anger expansion [5, 6],

$$\sin[z \sin(\Theta)] = 2 \sum_m J_{2m-1}(z) \cos\left[(2m-1)\Theta\right] \tag{S14}$$

where J_m is the Bessel function of m^{th} order, $z = \frac{eE_0 a}{\hbar\omega_0} = \frac{\omega_B}{\omega_0}$ and $\Theta = \omega_0 t$, to bring eq.(S13) to a more suitable form

$$v^{\parallel}(k_{\parallel}) = \frac{2\tilde{A}a}{\hbar} \sum_m J_{2m-1}\left(\frac{\omega_B}{\omega_0}\right) \cos\left[(2m-1)\omega_0 t\right], \tag{S15}$$

where $\omega_B = eE_0 a/\hbar$ is the Bloch frequency. Calculating the Fourier transform of eq. (S15) gives the third harmonic spectrum (for $m = 2$)

$$\mathcal{F}\left(v_{\nu}^{\parallel}(k_{\parallel})\right) \propto \overline{A}\left[\delta(\omega - 3\omega_0) + \delta(\omega + 3\omega_0)\right], \tag{S16}$$

where $\overline{A} = \sqrt{\frac{\pi}{2}} \frac{2\tilde{A}a}{\hbar} J_3\left(\frac{\omega_B}{\omega_0}\right)$. That describes the usual third harmonic generation without any modulation as expected. The goal is thus to integrate the electric field amplitude E_0 into the delta function, which automatically implies that the semiclassical momentum $\vec{k}(t)$ has to increase linearly in time.

5 Electron Motion in Solids - External Electric and Magnetic Field

Since the motion of an electron in an electric field only gives rise to usual third harmonic generation we also have to consider the possibility that the electron couples to the magnetic component of the driving field, in order to induce anharmonic modulation. Thus the Lorentzian force has to be included in which $\dot{\vec{r}} = \dot{x}_{\parallel}\vec{e}_x$ interacts with $\vec{B}(t)$. By means of the induction law

$$\mathrm{rot}\vec{E} = -\dot{B}(t) \tag{S17}$$

we can calculate the magnetic field

$$\vec{B}(t) = B_0 \cos(\omega_0 t - kz)\vec{e}_y \tag{S18}$$

with $B_0 = \frac{k}{\omega_0}E_0 = \frac{E_0}{c}$. The Lorentz force thus causes the electron to gain a motion in z-direction perpendicular to the electric and magnetic polarization

$$\begin{aligned} k_\perp \vec{e}_z = \frac{m^* \dot{x}_\perp}{\hbar}\vec{e}_z &= -\frac{e}{\hbar}\int_0^t dt'\, k_\parallel(t')\vec{e}_x \times \vec{B}(t')\vec{e}_z \\ \iff k_\perp \vec{e}_z &= \frac{eB_0}{m^*}\frac{eE_0}{\omega_0 \hbar}\int_0^t dt'\, \sin(\omega_0 t')\cos(\omega_0 t')\vec{e}_z \\ \iff k_\perp \vec{e}_z &= -\frac{\omega_c \omega_B}{2\omega_0^2 a}\cos^2(\omega_0 t)\vec{e}_z, \end{aligned} \tag{S19}$$

where $\omega_c = \frac{eB_0}{m^*}$ is the cyclotron frequency. Thus, undamped electron motion gives rise to a harmonic modulation of the electron momentum, which will have no effect on the spectral shifts observed in Fig 2d-f of the main text. This is due to the $\omega_0 t$-argument in the cosine function. Note that the coupling to the magnetic component according to eq. (S19) will induce a direct current since $-\frac{\omega_c\omega_B}{2\omega_0^2 a}\cos^2(\omega_0 t) = -\frac{\omega_c\omega_B}{2\omega_0^2 a}(1 - \sin^2(\omega_0 t))$. This direct current is important for the asymmetric harmonic yield of the nonresonant components $\lambda = 335\,\mathrm{nm}$ and $348\,\mathrm{nm}$ shown in Fig. 2f and in Fig. 3a in the main text, since it rotates the yield according to $e^{(i\omega_c\omega_B/2\omega_0^2)}$. Now, if $k_\perp\vec{e}_z$ according to

eq. (S19) is inserted into eq. (S15), the resulting velocity becomes:

$$v \propto \sin\left(\frac{\omega_B}{\omega_0}\sin(\omega_0 t) - \frac{\omega_B\omega_c}{2\omega_0^2}\cos^2(\omega_0 t)\right). \tag{S20}$$

This means that the goal of integrating the electric field strength into the delta function according to eq. (S16) is not achieved. For this, a linear relationship between the electron momentum k and time would be required. The velocity according to eq. (S15) would therefore have to take the following form:

$$v \propto \sin\left(\frac{\omega_B}{\omega_0}\sin(\omega_0 t) + bt\right), \tag{S21}$$

where $b \propto E_0^q$ with $q \geq 1$ must hold. Only in this case a spectral modulation by the external field can arise as described in the context of amplitude modulation. This will be possible in the damped case, as will be explained in the following (section 6).
Before that, Fig. S3 schematically summarizes how the individual electron momenta are composed. Fig. S3 a) shows the oscillation of the electric field. The magnet fields oscillating in phase to the electric field is shown in Fig. S3 b). The velocity induced by the electric field is shown in Fig. S3 c). It is phase-shifted relative to the electric and magnetic fields and corresponds to a sine oscillation. The cross product describing the Lorentz force, shown in Fig. S3 d), thus results from the product of a sine and a cosine oscillation. The temporal integration of this force in the k_z direction leads to a resulting electron momentum, which corresponds to a squared cosine oscillation. This is finally shown in Fig. S3 e).

6 Damped Electron Motion in Solids - External Electric and Magnetic Field

Since we generate the third harmonic in the vicinity of a charged vacancy with frequency Ω, the motion of an electron will further gain a damping term

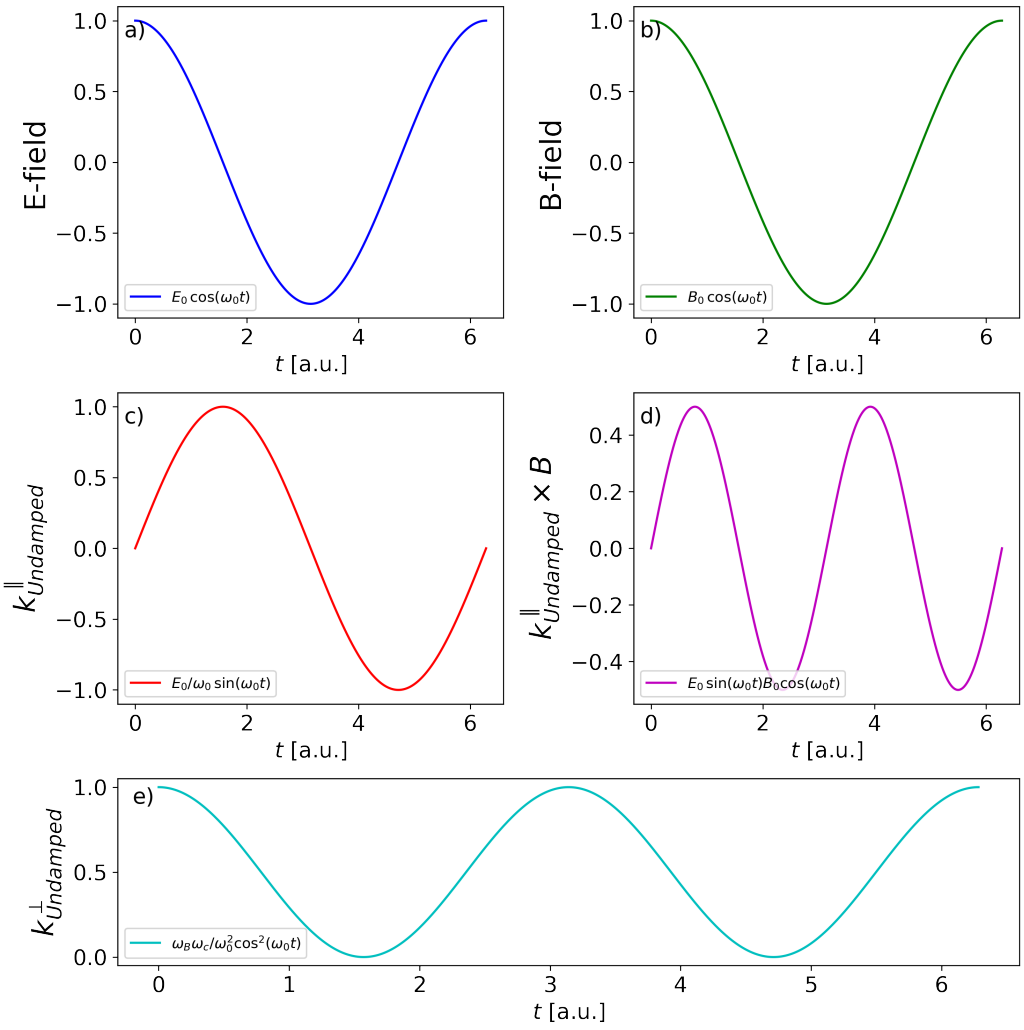

Figure S3: Schematic representation of the velocities and forces induced by the electric and magnetic fields in the undamped case: a) time evolution of the electric field, b) in-phase magnetic field, c) electron velocity induced by the electric field, d) resulting Lorentz force as the cross product of velocity and magnetic field, e) time-integrated electron momentum in the k_z direction, resulting in a squared cosine oscillation.

Γ which has to be included in the calculation. The equation of motion then will change to [7]

$$m^*[\ddot{x} + 2\Gamma\omega\dot{x} + \Omega^2 x] = -eE(t) \tag{S22}$$

with $E(t) = E_0 \cos(\omega_0 t) = \frac{1}{2}E_0 \left[\exp(i\omega_0 t) + \exp(-i\omega_0 t)\right]$. We can solve eq. (S22) with the approach

$$\begin{aligned} x_{\parallel,\mathrm{damp}} &= -\frac{eE_0}{2m^*}\left[\frac{\exp(i\omega_0 t)}{\Omega^2 - 2i\Gamma\omega_0 - \omega_0^2} + c.c.\right] \\ &= -\frac{eE_0}{2m^*}\left[\left(\frac{\exp(i\omega_0 t)(\Omega^2 - \omega_0^2)}{(\Omega^2 - \omega_0^2)^2 + (2\Gamma\omega_0)^2} - i\frac{2\Gamma\omega_0 \exp(i\omega_0 t)}{(\Omega^2 - \omega_0^2)^2 + (2\Gamma\omega_0)^2}\right) + c.c.\right]. \end{aligned} \tag{S23}$$

The complex conjugated part is given by

$$c.c. = \frac{\exp(-i\omega_0 t)(\Omega^2 - \omega_0^2)}{(\Omega^2 - \omega_0^2)^2 + (2\Gamma\omega_0)^2} + i\frac{2\Gamma\omega_0 \exp(-i\omega_0 t)}{(\Omega^2 - \omega_0^2)^2 + (2\Gamma\omega_0)^2}. \tag{S24}$$

By adding up eq. (S23) and eq. (S24) the time dependent location of the electron will gain a phase-shifted part compared to the undamped case

$$x_{\parallel,\mathrm{damp}} = -\frac{eE_0}{m^*}\frac{1}{(\Omega^2 - \omega_0^2)^2 + (2\Gamma\omega_0)^2}\left[(\Omega^2 - \omega_0^2))\cos(\omega_0 t) - 2\Gamma\omega_0 \sin(\omega_0 t)\right]. \tag{S25}$$

Note, when $\Omega, \Gamma = 0$ eq. (S25) becomes again eq. (S10) which describes the undamped case. In particular, the phase-shifted term $2\Gamma\omega_0 \sin(\omega_0 t)$ vanishes, which is crucial for the coupling to the magnetic field, as we will see below. The velocity of the damped electron can be calculated by taking the time derivative of eq. (S25) which results in

$$\dot{x}_{\parallel,\mathrm{damp}} = \frac{eE_0}{m^*}\frac{\omega_0}{(\Omega^2 - \omega_0^2)^2 + (2\Gamma\omega_0)^2}\left[(\Omega^2 - \omega_0^2))\sin(\omega_0 t) + 2\Gamma\omega_0 \cos(\omega_0 t)\right]. \tag{S26}$$

We already know from eq. (S19) and eq. (S14) that the left term in the squared brackets gives rise to only harmonic modulation. Therefore, only the right part will contribute to the interaction of the electron with the magnetic field. After applying the Lorentz force $\dot{x}_{\parallel,\mathrm{damp}}\vec{e}_x \times \vec{B}$ we get the

integral

$$k_{\perp,\mathrm{damp}}\vec{e}_z = \frac{m^*\dot{x}_{\perp,\mathrm{damp}}}{\hbar}\vec{e}_z = \frac{\omega_c\omega_B}{a}\frac{2\Gamma\omega_0^2}{(\Omega^2-\omega_0^2)^2+(2\Gamma\omega_0)^2}\cdot\int_0^t dt'\,\cos^2(\omega_0 t')\vec{e}_z. \tag{S27}$$

Using the approximation

$$\int_0^t dt'\,\cos^2(\omega_0 t') = \frac{t}{2}+\frac{\sin(2\omega_0 t)}{4\omega_0} \approx \frac{t}{2}. \tag{S28}$$

Since $\sin(2\omega_0 t) \in [-1,1]$ and $\omega_0 = 2\pi\cdot 291\,\mathrm{THz}$ the second term will contribute only non-significant noise to the motion and thus $\frac{\sin(2\omega_0 t)}{4\omega_0} \approx 0$. The momentum of the electron in $z-$direction is then given by

$$k_{\perp,\mathrm{damp}}\vec{e}_z = \frac{\omega_c\omega_B}{a}\frac{\Gamma\omega_0^2}{(\Omega^2-\omega_0^2)^2+(2\Gamma\omega_0)^2}\cdot t\vec{e}_z. \tag{S29}$$

Using the Fourier expansion of the band dispersion shown in eq.(S8) and (S12), a significant current in z-direction is induced by the damped velocity of the electron in a magnetic field

$$v_\nu^{\parallel} \approx -\frac{\tilde{A}a}{\hbar}\sin\left(\frac{\omega_B}{\omega_0}\sin(\omega_0 t)+\overline{\omega}t\right), \tag{S30}$$

with $\overline{\omega} = \omega_c\omega_B\frac{\Gamma\omega_0^2}{(\Omega^2-\omega_0^2)^2+(2\Gamma\omega_0)^2}$. That means that eq. (S21) is now satisfied. The left term $\frac{\omega_B}{\omega_0}\sin(\omega_0 t)$ is the electron momentum induced by solely the electric field of the driving pulse. The two momenta in different components are adding up due to the scalar product in eq. (S12). At this point, however, it must be considered that in this case there is no restoring force, so that $\Omega^2 x = 0$ can be set. The absence of a restoring force is due to the fact that these are intraband currents. Despite absorption at a resonance induced by the vacancy, the electrons are accelerated quasi-freely within the band. This is because $\hbar\omega_3 = 3.6\,\mathrm{eV} \ll E_g = 8.9\,\mathrm{eV}$. It thus corresponds to the Drude

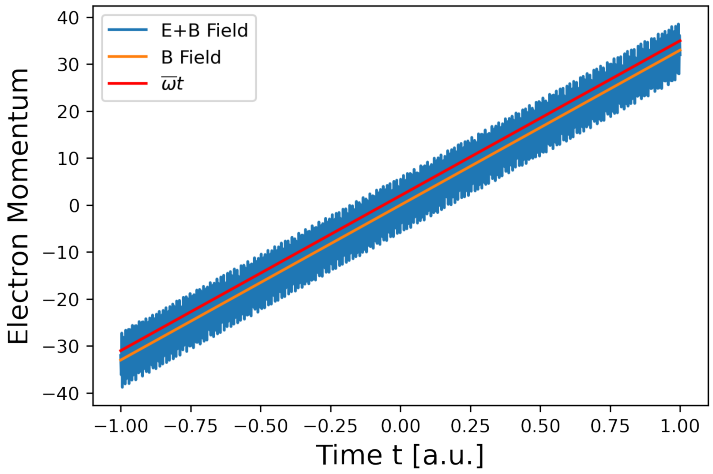

Figure S4: Electron momentum within an electromagnetic field. The blue, linearly increasing oscillation shows the electron momentum $\vec{k}\vec{a}$ induced by the electric and magnetic fields. The linear increase results from synchronization with the magnetic field component, while the superimposed high-frequency oscillation is caused by the electric field. The orange and red lines represent contributions to the momentum along the z-direction ($k_z a$) induced exclusively by the magnetic field. The orange line depicts the complete momentum including both synchronous and asynchronous components, while the red line only accounts for the linear term $\overline{\omega}t$. For better visibility, both lines have been slightly offset, although they are identical in content. It is evident that the harmonic modulations induced by the magnetic field are negligible in the significant region, so the linear component (red) is sufficient to describe the temporal momentum evolution.

model. Therefore, the modulation frequency $\overline{\omega}$ simplifies to

$$\overline{\omega} = \omega_c \omega_B \frac{\Gamma}{\omega_0^2 + (2\Gamma)^2}. \tag{S31}$$

According to the argument in eq. (S12) the complete electron momentum will be given by

$$\sum_i k_i a_i = \frac{\omega_B}{\omega_0} \sin(\omega_0 t) + \frac{\tilde{\omega}}{\omega_0} \cos^2(\omega_0 t) + \overline{\omega}t + \frac{\overline{\omega}}{2\omega_0} \sin(2\omega_0 t) \approx \frac{\omega_B}{\omega_0} \sin(\omega_0 t) + \overline{\omega}t \tag{S32}$$

with $\tilde{\omega} = \omega_c \omega_B \omega_0 \frac{\Omega^2 - \omega_0^2}{(\Omega^2 - \omega_0^2)^2 + (2\Gamma\omega_0)^2}$. Here the momenta induced by the electric

field, the synchronous coupling and asynchronous coupling to the magnetic component of the driving field were added up according to eqs. (S11), (S19), and (S29). We use the lattice constant of quartz which is $a = 5\,\text{Å}$. Fig. S4 shows the individual electron momenta. The total momentum according to eq. (S32) is shown in blue. To justify the linear approximation, the orange and red lines must be compared. These actually lie on top of each other, but in Fig. S4 they have been slightly offset for clarity. The red line represents the total momentum of the electrons in the k_z direction induced by the magnetic field, i.e., the $\frac{\tilde{\omega}}{\omega_0}\cos^2(\omega_0 t)$ term from eq. (S20) as well as the term $\left(\overline{\omega}t + \frac{\overline{\omega}}{2\omega_0}\sin(2\omega_0 t)\right)$ from the damped coupling. The orange line contains only the $\overline{\omega}t$ term from the damped coupling. Thus, there is no difference between these two curves. It is therefore immediately evident that the main contribution to the electron momentum is given by the last term in eq. (S32), and this approximation can thus be considered justified.
To calculate the spectrum of eq. (S30), we first have to use $\sin(A+B) = \sin(A)\cos(B) + \cos(A)\sin(B)$ with $A = \frac{\omega_B}{\omega_0}\sin(\omega_0 t)$ and $B = \overline{\omega}t$ to decompose eq. (S30). Thus, eq. (S30) changes to

$$\begin{aligned} v_\nu^{\parallel} &\approx -\frac{\tilde{A}a}{\hbar}\left[\sin\left(\frac{\omega_B}{\omega_0}\sin(\omega_0 t)\right)\cos(\overline{\omega}t) + \cos\left(\frac{\omega_B}{\omega_0}\sin(\omega_0 t)\right)\sin(\overline{\omega}t)\right] \\ &= -\frac{2\tilde{A}a}{\hbar}\sum_{m=1}^{\infty} J_{2m-1}\left(\frac{\omega_B}{\omega_0}\right)\sin\left((2m-1)\omega_0 t\right)\cos(\overline{\omega}t) - \\ &-\frac{2\tilde{A}a}{\hbar}\left[\frac{1}{2}J_0\left(\frac{\omega_B}{\omega_0}\right) + \sum_{m=1}^{\infty} J_{2m}\left(\frac{\omega_B}{\omega_0}\right)\cos(2m\omega_0 t)\sin(\overline{\omega t})\right]. \end{aligned} \tag{S33}$$

The second term of eq. (S33) only refers to even harmonics, so in our case, it will be neglected. The J_0 term can also be neglected, since it refers to a direct current. Note that the second term vanishes completely for $\overline{\omega} = 0$ and the first term remains. For odd harmonics we thus obtain for the velocity of the electron in the damped case

$$v_\nu^{\parallel} \approx -\frac{\tilde{A}a}{\hbar}\sum_{m=1}^{\infty} J_{2m-1}\left(\frac{\omega_B}{\omega_0}\right)\sin\left((2m-1)\omega_0 t\right)\cos(\overline{\omega}t) \tag{S34}$$

which is the mathematical formula for amplitude modulation. Therefore, the synchronization of the electron to the magnetic component of the driving field at a localized charge center will induce a new typ of opto-magnetic amplitude modulation of the harmonic spectra generated in the localized absorption region. Note that the amplitude modulation $\cos(\overline{\omega}t)$ only acts on harmonics m in the absorption region. For harmonics distant from this region $\cos(\overline{\omega}t) = 1$ because the $\overline{\omega} = 0$. The spectrum for the third harmonic in the spectral region where the charged vacancy shows absorption can be calculated using the Fourier transformation of eq. (S34)

$$\mathcal{F}[v_\nu^{\parallel}] \propto \frac{\tilde{A}a}{\hbar} \sum_{m=1}^{\infty} J_3\left(\frac{\omega_B}{\omega_0}\right) \delta(\omega - 3\omega_0 \pm \overline{\omega}) \tag{S35}$$

Since $\overline{\omega} \propto E_0^2$ the goal to put the electric field into the $\delta-$function is achieved. The field dependent frequency modulation can be thus explained by eq. (S35). Fig. S5 provides a summary of the schematic development of the calculation for the damped case. Fig. S5 a) and b) correspond to the electric and magnetic fields, as already shown in Fig S3 a) and b). The damped electron momentum, shown in Fig. S5 c), is now in phase with the electric and magnetic fields and also corresponds to a cosine oscillation. Therefore, the cross product shown in Fig. S5 d) results in a squared cosine oscillation, so that after temporal integration of the cross product, a linearly increasing momentum in the k_z direction arises, as shown in Fig. S5 e).
For $m^* = 0.055m_e$, $\omega_0 = 2\pi \cdot 291\,\mathrm{THz}$, $\Gamma = 2\pi \cdot 70\,\mathrm{THz}$ ($\approx 0.3\,\mathrm{eV}$) [1], $E_0 = 1.4\,\mathrm{V/Å}$, and $B_0 = 46\,\mathrm{T}$, the frequency shifts to $\overline{\omega} \approx 2\pi \cdot 24.0\,\mathrm{THz}$. The Bloch frequency is $\omega_B \approx 11\,\mathrm{PHz}$, and the cyclotron frequency is $\omega_c \approx 147\,\mathrm{THz}$.
Now, eq. (S31) must be verified. A closer look at the spectra from Fig. 2e and f reveals that a frequency shift relative to the resonant third harmonic at $\lambda = 343\,\mathrm{nm}$ is not sufficient, since an additional spectral modulation dependent on the azimuth is observed. In the previous calculation the crystal symmetry is neglected. Therefore the reference frequency will be different for the blue- and red-shifted components. Considering the spectrum, shown in Fig. 2 d and f, one observes, as previously mentioned, an S-shaped modulation in

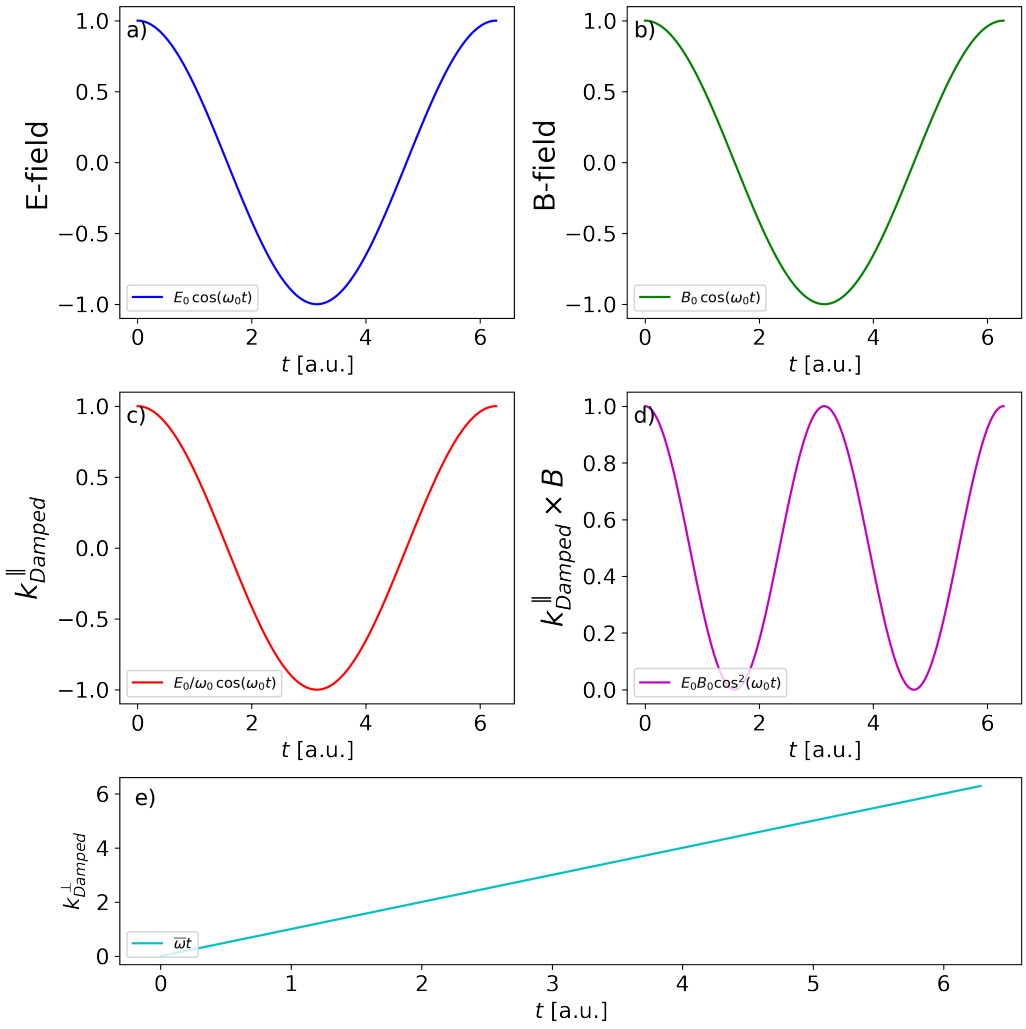

Figure S5: Schematic representation of the velocities induced by the electric and magnetic fields in the damped case. a) shows the oscillation of the electric field. The corresponding in-phase magnetic field is shown in b). The electron momentum induced by the electric field, now damped, is shown in c). It is in phase with the electric and magnetic fields and corresponds to a cosine oscillation. The cross product of the velocity with the magnetic field, shown in d), therefore results in a quadratic cosine oscillation. After time integration of the cross product, a linearly increasing momentum in the k_z-direction arises, as shown in e).

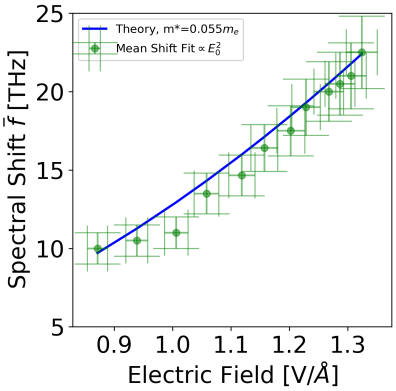

Figure S6: Mean value of the pump-field-dependent blue and red spectral shifts for the z-cut.

the azimuth. The suppression of the resonant harmonic does not appear as a continuous resonant line across the spectrum. For the suppressed reference frequency, the red spectral components use the component at $\lambda = 339\,\mathrm{nm}$, while the resonant harmonic at $\lambda = 343\,\mathrm{nm}$ serves as the suppressed reference frequency for the blue components. This can be exemplified at the positions $\alpha \approx 30°$ (redshift) and $\alpha \approx 0°$ (blueshift).
Fig. S6 shows the field-dependent shifts for the z-cut. From these, an effective mass of $m^* \approx 0.055\,m_e$ can be derived. An overall quadratic dependence on the field strength E_0 is recognizable.

7 Momentum-Space Dependent Amplification

Until now, the initial electron momentum was assumed to be zero. However, this assumption is not valid within a crystal's Brillouin zone. Therefore, a non-zero electron momentum [5, 8, 9] at $t = 0$ also couples to the magnetic part of the laser as

$$\begin{aligned} k_{\perp,\mathrm{initial}}(t)\vec{e}_z &= -\frac{e}{m^*}B_0 \int_0^t dt'\, k(0)_{\parallel,\mathrm{solid}}\vec{e}_x \times \cos(\omega_0 t')\vec{e}_y \\ \iff k_{\perp,\mathrm{initial}}(t)\vec{e}_z &= -\frac{\omega_c}{\omega_0}k(0)\sin(\omega_0 t)\vec{e}_z, \end{aligned} \tag{S36}$$

where $k(0)$ is the non-zero momentum of the electron in the Brillouin zone. Also the non-zero initial momentum in $z-$direction couples to the magnetic component (see main text) giving rise to a contribution in x-direction due to the cross product. Here, we will set this one to zero for simplicity. Thus, the momentum of the electron changes to

$$\sum_i k_i a_i = \frac{\omega_B}{\omega_0}\sin(\omega_0 t) \pm \overline{\omega} t - \frac{\omega_c}{\omega_0} k(0) a \sin(\omega_0 t) \tag{S37}$$

Using the Jacobi-Anger expansion

$$\exp\left[iz\sin(\Theta)\right] = \sum_m J_m(z)\exp\left[im\Theta\right], \tag{S38}$$

we can rewrite the new current to

$$\tilde{A}\exp\left[i\left(\frac{\omega_B}{\omega_0} - \frac{\omega_c}{\omega_0}k(0)\,a\right)\sin(\omega_0 t)\right] = \sum_m \tilde{A}\; J_m\left(\frac{\omega_B}{\omega_0} - \frac{\omega_c}{\omega_0}k(0)\,a\right)\exp\left[im\omega_0 t\right]. \tag{S39}$$

From Fig. S7 it is obvious, that the measured spectra differ from the fit obtained by eq. (S39). This is due to the fact that the damping of the electron is not a feature of the band dispersion according to eq. (S8) but occurs rather at localized points. Thus, another method has to be used to include the damping induced by the localized vacancy centers. We have to note, that the resonant Harmonic $\lambda = 343\,\mathrm{nm}$ shown in Fig. S7 can be fitted using higher harmonics $\tilde{n}$ from eq. (S12). However, the non-resonant parts or in other word, the complete spectrum is not reconstructable with eq. (S39) with higher harmonics of the band dispersion $\tilde{n}$.
The Bloch functions are plane waves in momentum space and are thus delocalized. Therefore, a change in basis is needed.

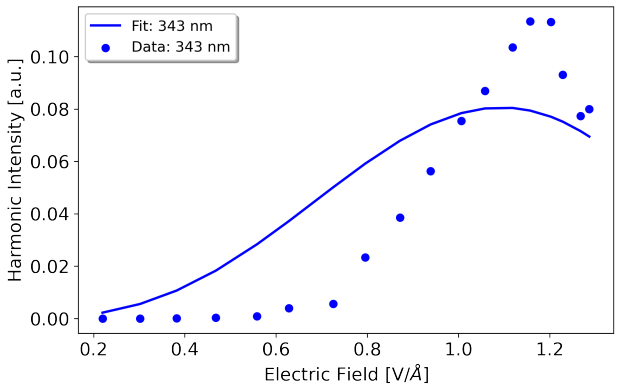

Figure S7: Fitted function according to eq. (S39) to one spectral component of the z-cut. The fit function and the measured data do not match.

8 Maximally localized Wannier states

Since the charge centers are localized states, they can be described by a Wannier representation. We consider the following matrix element [10]

$$M_{n',n}(k',k) = \langle n'k'|B|nk\rangle, \tag{S40}$$

with some matrix B. The Bloch states $\langle x|nk\rangle = u_{nk}(x)$ can be expressed via maximally localized Wannier states (MLWS) $|jR\rangle$ [11]

$$|nk\rangle = \sum_{jR} e^{ikR}\, U^{\dagger}_{jn,k}|jR\rangle \tag{S41}$$

and

$$|jR\rangle = \frac{1}{N_k}\sum_{nk} e^{-ikR}\, U_{nj,k}|nk\rangle \tag{S42}$$

where U, $U^{\dagger}$ is the unitary matrix that describes the maximal localization according to

$$|nk\rangle = \sum_{n'} U_{n'n,k}|n'k_0\rangle, \tag{S43}$$

where N_k is the number of $k-$points in the BZ. Thus, the matrix element can be written as

$$M_{j',j}(R',R) = \langle j'R'|B|jR\rangle = \frac{1}{N_k}\sum_{n'nk} e^{-ik\Delta R}\, U^{\dagger}_{n'j',k}\langle n'k|B|nk\rangle U_{jn,k}, \quad \text{(S44)}$$

where $\Delta R = R' - R$ denotes the spacing of two Wannier sates. For $B = \nabla_k$ and $n' = n$, eq. (S44) can be related to the Berry connection $A_n(k) = i\langle nk|\nabla_k|nk\rangle$ and the Berry phase $\gamma_n = i\oint dk\langle nk|\nabla_k|nk\rangle$. They can be directly connected to a polarization term [12]

$$P = \frac{e}{(2\pi)^3}\Im\left(\sum_n i\int dk\langle nk|\nabla_k|nk\rangle\right). \quad \text{(S45)}$$

In order to calculate the emitted harmonic spectra modulated at a vacancy, we have to calculate the Fourier transform of a current $j(t) = \frac{d}{dt}P(t)$. Our basis will be time-dependent and we can use the adiabatic theorem

$$|n(t)\rangle = \sum_{n'} c_{n'n}(t)|n'(t)\rangle, \quad \text{(S46)}$$

with $c_{n'}(t) = c_{n'}(0)e^{i\theta_{n'}(t)}e^{i\gamma_{n'}(t)}$ is the transition probability. Here

$$\theta_{n'} = -\frac{1}{\hbar}\int_0^t E_{n'}(t')dt' \quad \text{(S47)}$$

denotes the dynamical phase and

$$\gamma_{n'} = i\int_0^t \langle n'(t')|\dot{n'}(t')\rangle dt' \quad \text{(S48)}$$

the geometrical phase. In particular the system remains in the eigenstate at $t = 0$ and only exhibits a change in phase. Thus, the probability amplitudes remain the same over time for intraband currents, since the phases in the adiabatic expansion vanish when taking the square of the wavefunction. The

transition amplitude thus is given by

$$|c_{n'}(t)|^2 = |c_{n'}(0)|^2. \tag{S49}$$

We can now rewrite eq. (S45) in a time-dependent basis

$$P(t) = \frac{e}{(2\pi)^3}$$
$$\Im\left(i\sum_{n'n}\int d(k_0+k(t))c^*_{n'}(t)c_n(t)\langle n'(t),k_0+k(t)|\nabla_{k_0+k(t)}|n(t),k_0+k(t)\rangle\right) \tag{S50}$$

with $k \to k_0 + k(t)$ and having ignored the phase factors for this particular problem. For an intraband polarization this simplifies to [9]

$$P(t)^{\text{intra}} = \frac{e}{(2\pi)^3}$$
$$\Im\left(i\sum_{n}\int d(k+k(t))|c_n(0)|^2\langle n(t),k_0+k(t)|\nabla_{k_0+k(t)}|n(t),k_0+k(t)\rangle\right) \tag{S51}$$

Combining eq.(S44) and eq. (S51) our time-dependent polarization term for a maximally localized current can be written as

$$P(t)^{\text{intra,loc}} = \frac{e}{(2\pi)^3}\Im\left(i\sum_{n}\int d(k_0+k(t))|c_n(0)|^2 e^{-i(k_0+k(t))\Delta R}\right.$$
$$\left. U^\dagger_{n,k_0+k(t)}\langle n(t),k_0+k(t)|\nabla_{k_0+k(t)}|n(t),k_0+k(t)\rangle U_{n,k_0+k(t)}\right) \tag{S52}$$

In order to remove the time dependency from the matrix elements we use the definition of the unitary matrix and the adiabatic theorem

$$\langle n(t)|n(t)\rangle = \langle n(0)|U^\dagger(t_0,t)U(t_0,t)|n(0)\rangle = \langle n(0)|n(0)\rangle = \langle n|n\rangle, \tag{S53}$$

since $U^\dagger(t_0,t)U(t_0,t) = 1$. For $|k_0+k(t)\rangle$ the same rules can be applied using

eq. (S43). For a time dependent operator $A(t)$, the unitary transformation

$$A(t) = U^{\dagger}(t_0, t)A(0)U(t_0, t) \tag{S54}$$

is valid and $\nabla_{k_0+k(t)} \to \nabla_{k_0}$. Thus, the maximally localized polarization can be rewritten as

$$P(t)^{\text{intra,loc}} = \frac{e}{(2\pi)^3}$$
$$\Im\left(i\sum_n \int d(k_0 + k(t))|c_n(0)|^2 e^{-i(k_0+k(t))\Delta R} U^{\dagger}_{n,k_0}\langle nk_0|\nabla_{k_0}|nk_0\rangle U_{n,k_0}\right). \tag{S55}$$

Since $dk \to d(k_0 + k(t))$ as $k \to k_0 + k(t)$, the differential changes to the sum $dk_0 + dk(t)$. The second term $dk(t) = \frac{\partial k(t)}{\partial t}dt$ changes to a total differential. It is a line integral, and it is well known that these type of integrals will always depend on the initial and final point (T_i, T_r, where T_i is the ionization time and T_r is the recombination time) and not on the path itself. Thus, this part of the polarization will not depend on time. So the current

$$\frac{d}{dt}P(T_i, T_r)^{\text{intra,loc}} \propto$$
$$\propto \frac{d}{dt}\Im\left(\int_{T_i}^{T_r} dt\left(\frac{\partial k(t)}{\partial t}\right) e^{i(k_0+k(t)\Delta R} U^{\dagger}_{n,k_0}\langle nk_0|\nabla_{k_0}|nk_0\rangle U_{n,k_0}\right) = 0 \tag{S56}$$

will not contribute to the spectral power density. The final time-dependent polarization is

$$P(t)^{\text{intra,loc}} = \frac{e}{(2\pi)^3}$$
$$\Im\left(i\sum_n \int_{BZ} dk_0|c_n(0)|^2 e^{-i(k_0+k(t))\Delta R} U^{\dagger}_{n,k_0}\langle nk_0|\nabla_{k_0}|nk_0\rangle U_{n,k_0}\right). \tag{S57}$$

Now, we have to find a value for ΔR. Since we operate in reciprocal space it

will be a fixed value. For $\Delta R > a$ the matrix element

$$U^{\dagger}_{n,k_0} \langle nk_0 | \nabla_{k_0} | nk_0 \rangle U_{n,k_0} \tag{S58}$$

will rapidly decay to zero, since it is maximally localized. For $\Delta R = 0$ the time dependency of $P(t)^{\text{intra,loc}}$ will vanish and thus the current $j = \frac{d}{dt} P(t)^{\text{intra,loc}} \to 0$. From the frequency shift according to $\overline{\omega}$ and the time-bandwidth product for a pulse of $\tau = 40\,\text{fs}$ ($\Delta\nu = 11\,\text{THz}$) we can estimate a lower limit for ΔR

$$\frac{\overline{f}}{a} \Delta R < 11\,\text{THz}. \tag{S59}$$

For a maximum frequency shift of $\overline{f}_{\max} \approx 22\,\text{THz}$ the lower limit approaches approximately

$$\Delta R_{\min} \approx \frac{a}{2}. \tag{S60}$$

However, only the upper limit for $\Delta R = a$ has to be taken into account, since it has the more dominant contribution for the harmonic yield due to eq. (S39) and there are no atoms for values for $\Delta R < a$. For a total electron momentum of

$$\vec{k}(t) = \left(\frac{\omega_B}{a\omega_0} - \frac{\omega_c}{\omega_0} k_0 \right) \sin(\omega_0 t) \vec{e}_x + \frac{\overline{\omega}}{a} t \vec{e}_z, \tag{S61}$$

and the polarization according to eq. (S55) for $\Delta R_{\max} = a$, we can rewrite the new current using the same splitting as in eq. (S33), since the polarization is given by the imaginary part to

$$\begin{aligned} j(t) &\propto \frac{d}{dt} \sum_{k_0} A_n(k_0) \sin\left[\left(\frac{\omega_B}{\omega_0} - \frac{\omega_c}{\omega_0} k_0 a \right) \sin(\omega_0 t) \right] \cos(\overline{\omega} t) = \\ &= \frac{d}{dt} \sum_{k_0} A_n(k_0) J_3 \left(\frac{\omega_B}{\omega_0} - \frac{\omega_c}{\omega_0} k_0 \cdot a \right) \sin(3\omega_0 t) \cos(\overline{\omega} t), \end{aligned} \tag{S62}$$

where $A_n(k_0)$ is the Berry connection of band n. From this equation it is clear that the Berry connection can be extracted from the field dependend spectra generated in the vicinity of the localized vacancy center. In particular, the spectrum is given by the Fourier transform of eq. (S62). Fig. S8 displays

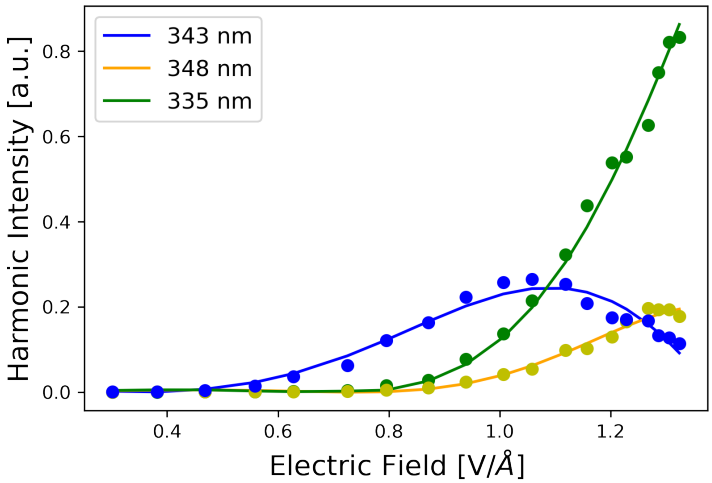

Figure S8: Harmonic gain for three wavelengths plotted with eq. (S62) for the z-cut. The points represent the experiment and the lines denote the theory.

the one dimensional cuts of three different spectral components for the z-cut, respectively. The fit function according to eq. (S62) matches the observed spectra. Note, that the Berry connection is a gauge dependent quantity and is therefore usually not referred as physical observable. The overall Fourier transformation of eq. (S62) is given by

$$\begin{aligned} j(\omega) \propto \sum_{k_0} A_n(k_0) J_3 \left(\frac{\omega_B}{\omega_0} - \frac{\omega_c}{\omega_0} k_0 \cdot a \right) \frac{1}{2} \sqrt{\frac{\pi}{2}} \left[(3\omega_0 + \overline{\omega}) \delta(3\omega_0 + \overline{\omega} - \omega) \right. \\ \left. + (3\omega_0 - \overline{\omega}) \delta(3\omega_0 - \overline{\omega} - \omega) \right] + \\ + \sum_{k_0} A_n(k_0) J_3 \left(\frac{\omega_B}{\omega_0} - \frac{\omega_c}{\omega_0} k_0 \cdot a \right) \frac{1}{2} \sqrt{\frac{\pi}{2}} \left[(3\omega_0 + \overline{\omega}) \delta(3\omega_0 + \overline{\omega} + \omega) \right. \\ \left. + (3\omega_0 - \overline{\omega}) \delta(3\omega_0 - \overline{\omega} + \omega) \right] . \end{aligned} \tag{S63}$$

9 Fitting of the Berry Connection

In this work, we employed the Levenberg-Marquardt (LM) method for non-linear least-squares fitting using Python. To improve the stability and con-

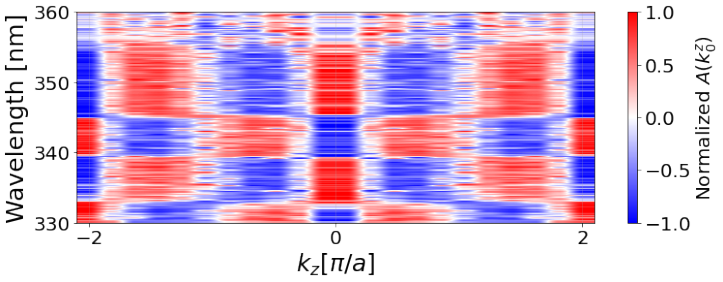

Figure S9: Normalized Berry connection for the z-cut

vergence of the algorithm, we manually adjusted the parameter space by introducing additional, unused parameters. These "empty" parameters, while not explicitly contributing to the functional form of the model, acted to enhance the distribution of the eigenvalues of the Jacobian matrix, effectively improving the conditioning of the problem. Consequently, this led to a better adjustment of the damping parameter λ during the optimization process, resulting in a more stable fit.

From eq. (S62) we know that the Berry connection parallel to the propagation direction can be extracted from the measured third harmonic spectra. We sample the whole Brillouin zone between $-\frac{\pi}{a}$ and $\frac{\pi}{a}$ or between 0 and $\frac{2\pi}{a}$ with a step size of $0.1/\text{Å}$. Due to time reversal (parity) symmetry $\mathcal{T}(\mathcal{P})$ the Berry connection is a symmetrical function, which is valid for a crystal with broken inversion symmetry. Our regression of the spectra implies [13, 14]

$$A(k_0^z) = A(-k_0^z). \tag{S64}$$

Fig. S9 displays the Berry connection for z-cut for an integration range of $[0, \frac{2\pi}{a}]$. The resulting spectra are shown in Fig. 3 b), d), and f) in the main text. The Berry connection obtained with a symmetric integration range ($[-\frac{\pi}{a}, \frac{\pi}{a}]$) for the z-cut is shown in Fig. S17. Different spectral components exhibit a sign flip in their extracted Berry connection.

10 Wannier-Stark Localization

The generated spectra for the z-cut are shown in Fig. 2 d-f, particularly as a function of the azimuthal rotation of the crystal. In addition, Fig. 3 in the main text provides a detailed description and reconstruction of the field-dependent amplification. Differences from the conventional description of harmonic generation have been identified. Some of these deviations could already be explained within the framework of the plane-wave approximation using the semiclassical approach of synchronization of the electron velocity with the magnetic field of the driving field, as well as through localized Wannier states. Nevertheless, several phenomena remain unexplained, while the analysis of the Berry connections has revealed additional new characteristics. These open questions will be addressed in the following sections. First, however, the properties of the Berry connections will be examined in more detail. A central feature is the observed systematic sign change, which becomes particularly apparent in the analysis.

It is now established that the Berry connection can be extracted from the measured spectra. However, to understand the observed systematic sign reversal, it is first necessary to recapitulate what the Berry connection describes in a physical context. For solids, the Berry connection was introduced in section 8 using localized Wannier functions and the connection to macroscopic polarization in solids was established. A detailed discussion of this can be found in [11]. The sum over the Berry connections in k-space corresponds to an intraband current. This means that the harmonics under consideration are generated within a single band, without transitions to other bands. This interpretation is particularly relevant, as the third harmonic investigated here lies within the band gap of quartz, thus ruling out interband-induced transitions.

It is now striking that the normalized Berry connections, particularly for the resonant component and the opto-magnetically modulated spectral components, exhibit opposite signs. This suggests that these components may not originate within the same band and that a simple intraband model may be insufficient to fully describe the generation of these sub-band-gap harmonics.

Furthermore, some of these spectral components show a significant increase in amplitude depending on the external field strength E_0. This could indicate that the underlying dynamics take place in the conduction band, while other components may be generated in the valence band. To analyze these processes in more detail, a two-level model encompassing both the valence and conduction bands will be considered in the following. Therefore we start with band deformation induced by an external electric field. This is known as Wannier-Stark localization.

When an strong optical pulse passes through a wide-band gap crystal, it will bent the band structure of the crystal [15–17]. Thus the energy eigenstates E_n of band n of the crystal will be bend by the Wannier-Stark shifts. They form the so-called Wannier-Stark ladder [15]:

$$E_{n,l} = E_n - \hbar\omega_B l \tag{S65}$$

with $l = -\tilde{n}_{\max}/2, ..., \tilde{n}_{\max}/2$. For our case $\tilde{n}_{\max} = 1$. The band gap reduces to

$$E_{c,-1/2} - E_{v,1/2} = E_c - E_v - \hbar\omega_B. \tag{S66}$$

Thus the valence band will be shifted upwards and the conduction band will be shifted downwards. The other case in which the valence band is shifted downwards and the conduction band is shifted upwards is not of interest here. For $E_0 = 1.4\,\mathrm{V/Å}$ the Bloch energy will be $\hbar\omega_B = 7.24\,\mathrm{eV}$. The length of a Wannier-Stark localization is given by [15]

$$L_{\mathrm{WS}} = \frac{\hbar^2}{m_e^* a^2 |eE_0|} \tag{S67}$$

and thus, the effective mass for a length of $L_{\mathrm{WS}} = a$ can be determined by

$$m_e^* = \frac{\hbar^2}{a^3 |eE_0|} \tag{S68}$$

as $m_e^* \approx 0.044\, m_e$ for a field strength of $E_0 = 1.4\,\mathrm{V/Å}$. This is in good agreement with the effective mass determined here, which is approximately $m_e^* \approx 0.055 - 0.06\, m_e$, as shown in Fig. S6.

11 Avoided Crossing

Consider a two-level quantum system described by the Hamiltonian

$$H = \begin{pmatrix} E_1 & 0 \\ 0 & E_2 \end{pmatrix}, \tag{S69}$$

where E_1 and E_2 are the energy eigenstates of $|\psi_1\rangle$ and $|\psi_2\rangle$ shown in Fig. 5b in the main text. For $E_1 = E_2$ the energy eigenvalues are degenerate. If we assume, that a perturbation H_{int} acts on the off-diagonal elements as V, the new Hamiltonian $H^{'} = H + H_{\mathrm{int}}$ can be written as

$$H^{'} = \begin{pmatrix} E_1 & V \\ V & E_2 \end{pmatrix}. \tag{S70}$$

The new eigenvalues of the Hamiltonian, representing the energy levels of the system, are given by

$$E_{\pm} = \frac{E_1 + E_2}{2} \pm \sqrt{\left(\frac{E_1 - E_2}{2}\right)^2 + V^2}. \tag{S71}$$

In the absence of coupling ($V = 0$), the energy levels cross when $E_1 = E_2$. However, for $V \neq 0$, the term V^2 ensures that the levels avoid crossing, resulting in a minimum energy gap $2V$. To find the new eigenstates of these eigenvalues, we can write the new eigenstates as a superposition of the old states $|\psi_1\rangle$ and $|\psi_2\rangle$

$$|\psi_+\rangle = \cos\left(\frac{\theta}{2}\right)|\psi_1\rangle + e^{i\phi}\sin\left(\frac{\theta}{2}\right)|\psi_2\rangle \tag{S72}$$

$$|\psi_-\rangle = -e^{-i\phi}\sin\left(\frac{\theta}{2}\right)|\psi_1\rangle + \cos\left(\frac{\theta}{2}\right)|\psi_2\rangle. \tag{S73}$$

These two new states are an orthonormal basis. So

$$\langle \psi_{\mp} | \psi_{\pm} \rangle = 0, \ \langle \psi_{\mp} | \psi_{\mp} \rangle = 1 \tag{S74}$$

is valid. It is well known, that these two states have Berry connections and thus Berry phases which are opposite in sign (as we have in our measurements). The Berry phase γ for these two states is given by

$$\gamma_{\pm} = \mp \frac{\Omega_B}{2}, \text{ with } \Omega_B = 2\pi(1 - \cos(\theta)). \tag{S75}$$

The angle θ is given by

$$\tan(\theta) = \left(\frac{2V}{E_1 - E_2} \right). \tag{S76}$$

The states $|\psi_{\pm}\rangle$ are entangled.

12 Landau-Zener Tunnel Effect

An important application of the adiabatic/diabatic avoided crossing theorem is the Landau-Zener tunnel effect. It describes the probability of tunnelling from the lower state ψ_- to the upper state ψ_+ when an external field is applied. The starting point of such systems is a Hamiltonian which time-dependence is linearly in time

$$H^{'} = H_{\text{int}} + H = H_{\text{int}} + At = \begin{pmatrix} E & V \\ V & -E \end{pmatrix} = \begin{pmatrix} \tilde{\alpha}t & V \\ V & -\tilde{\alpha}t \end{pmatrix}, \tag{S77}$$

where $E = E_1 = -E_2 = \tilde{\alpha}t$. At $t = 0$ the two states E_1 and E_2 would be degenerate without the perturbation H_{int}. But due to this perturbation, avoided crossing occurs and the two states have a band gap of $2V$. The transition/tunnel probability at $t = 0$ is given by

$$P = \exp(-2\pi\Gamma). \tag{S78}$$

The factor Γ is given by

$$\Gamma = \frac{|\langle\psi_+|H_{\text{int}}|\psi_-\rangle|^2}{\hbar\frac{\partial E}{\partial t}}, \tag{S79}$$

where $\langle\psi_+|H_{\text{int}}|\psi_-\rangle = V$ denotes the energy gap.

13 Landau-Zener in Solids - Synchronization to the Magnetic Field

In solids, the Landau-Zener-Hamiltonian is given by

$$H'_{\text{Solids}} = \begin{pmatrix} \frac{p}{m}\hbar k & \frac{1}{2}E_g \\ \frac{1}{2}E_g & -\frac{p}{m}\hbar k \end{pmatrix} \tag{S80}$$

Due to the synchronization of the localized damped electron velocity p/m to the magnetic component of the seed pulse and considering a one-dimensional problem only in z-direction, the electron momentum can be replace by $k_z = \overline{\omega}/a \cdot t$. Thus, the Hamiltonian can be written as

$$H'_{\text{Solids}} = \begin{pmatrix} v_k\hbar\overline{\omega}/a \cdot t & \frac{1}{2}E_g \\ \frac{1}{2}E_g & -v_k\hbar\overline{\omega}/a \cdot t \end{pmatrix}, \tag{S81}$$

leading us directly to the linear Landau-Zener effect given above. The transition probability factor Γ is given by

$$\Gamma = \frac{|E_c(k=0) - E_v(k=0) - \hbar\omega_B|^2}{v_k\hbar^2\frac{2\overline{\omega}}{a}} \tag{S82}$$

Here $k = t = 0$ means the energy gap at the Γ point, since $|\psi_+\rangle = |u_{c,k}\rangle$ is the conduction band and $|\psi_-\rangle = |u_{v,k}\rangle$ is the valence band. In eq. (S28) there is an additional term to the linear one which we left out due to its minimal effect on the electron momentum shown in fig. S4. However, since we look at the derivative at $t = 0$ and only in z-direction the second term $\propto \sin(2\omega_0 t)$ has also to be taken into account given an additional factor of 2

in eq. (S82).

Due to the substitution $k_z = \frac{\varpi}{a}t$, the linear dependence in time according to eq. (S77) is satisfied. According to eq. (S72) and (S73), the valence and the conduction bands are the described two entangled states. The Berry connections shown in Fig.S9 exhibit opposite signs. Therefore, the modulated, non-resonant harmonics are not generated as intraband current in the valence band, but rather as intraband current in the conduction band. If this is the case, the amplification of the modulated, non-resonant harmonics should be proportional to the tunnelling probability of the Landau–Zener tunnelling effect according to eq. (S82). This is indeed the case. Fig. 5d shows the fit of eq. (S82) to the normalized intensity of the opto-magnetically modulated components, exemplified for the z-cut. The resulting effective mass, obtained from the Landau–Zener tunnelling effect through the Brillouin momentum $v_k = 2\hbar\pi/(am^*)$, is approximately $m^* \approx 0.04\, m_e$ for a constant effective mass, and $m^* \approx 0.02\, m_e$ for an electric-field-dependent effective mass according to eq. (S68) at a field strength of $E_0 \approx 1.4\,\mathrm{V/Å}$. This agrees well with the assumption of a strongly reduced effective mass due to Wannier–Stark localization, as given by eq. (S68). However the field dependent reduction in effective mass should be also checked as fitting parameter in eq. (S62). This will be discussed in more detail later. However, according to eq. (S76) and the fact that tunnelling occurs at $t = 0$, the two states E_1 and E_2 become degenerate. As a result, the Berry phase takes a fixed value of $\pi/2$, and the θ-dependence described by eq. (S75) cannot be reproduced. This raises the question of whether it is possible to reconstruct the θ-dependence of the Berry phase for the valence and conduction bands based on the states $\psi_\pm$ given in eqs. (S72) and (S73) using the measured spectra. The answer is yes. To achieve this, one must perform a basis transformation and analyse how the Berry connections and Berry phases—induced by the synchronization of the electron velocity with the magnetic component of the driving field—relate to those of the two Bloch states $\psi_\pm$.

14 Topological Connection between the Bloch sphere and the Brillouin zone

Due to eq. (S76), the angle θ is fixed at $\theta = \pi/2$, resulting in a constant Berry phase of $\gamma_\pm = \mp\pi$. This follows from the fact that tunnelling occurs at $t = 0$, where the two states E_1 and E_2 are degenerate, leading to $E_1 - E_2 = 0$ and consequently fixing the value of θ.
To express the Berry phase $\gamma_\pm = \pi(1 - \cos\theta)$ of the two states $|\psi_\pm\rangle$, a basis transformation is required. It is therefore useful to calculate the Berry phase of the entangled pseudo-spin states to understand how the Brillouin zone coordinates in reciprocal space connect to the parametric coordinates (θ, ϕ) of the Bloch sphere. The spherical coordinates are given by

$$\begin{aligned} \tilde{x} &= \tilde{r}\sin\theta\cos\phi, \\ \tilde{y} &= \tilde{r}\sin\theta\sin\phi, \\ \tilde{z} &= \tilde{r}\cos\theta. \end{aligned} \tag{S83}$$

The angle ϕ ranges from $[0, 2\pi]$, while θ can take values in either $[-\pi/2, \pi/2]$ or alternatively in $[0, \pi]$. Consequently, only the angle ϕ can serve as a closed path for the Berry phase calculation.
The state $|\psi_+\rangle$ is given by

$$|\psi_+\rangle = \cos\left(\frac{\theta}{2}\right)|\psi_1\rangle + e^{i\phi}\sin\left(\frac{\theta}{2}\right)|\psi_2\rangle. \tag{S84}$$

Taking its gradient yields

$$\nabla|\psi_+\rangle = -\sin\left(\frac{\theta}{2}\right)\frac{d\theta}{2}|\psi_1\rangle + ie^{i\phi}\sin\left(\frac{\theta}{2}\right)d\phi|\psi_2\rangle + e^{i\phi}\cos\left(\frac{\theta}{2}\right)\frac{d\theta}{2}|\psi_2\rangle. \tag{S85}$$

Multiplying eq. (S85) by $\langle\psi_+|$ results in

$$\begin{aligned}\langle\psi_+|\nabla|\psi_+\rangle &= -\cos\left(\frac{\theta}{2}\right)\sin\left(\frac{\theta}{2}\right)\frac{d\theta}{2} + \sin\left(\frac{\theta}{2}\right)\cos\left(\frac{\theta}{2}\right)\frac{d\theta}{2} + i\sin^2\left(\frac{\theta}{2}\right)d\phi \\ &= i\sin^2\left(\frac{\theta}{2}\right)d\phi = \frac{i}{2}(1-\cos\theta)d\phi. \end{aligned} \tag{S86}$$

Thus, the $d\theta$ integration vanishes entirely, leaving only the $d\phi$ integration to contribute to the Berry phase, as expected from the definition range of the polar angles in eq. (S83). The Berry phase of the upper state $|\psi_+\rangle$ is then calculated as

$$\gamma_+ = \int_0^{2\pi} i\langle\psi_+|\nabla|\psi_+\rangle d\phi = -\pi(1-\cos\theta). \tag{S87}$$

A similar calculation applies to the lower state:

$$|\psi_-\rangle = -e^{-i\phi}\sin\left(\frac{\theta}{2}\right)|\psi_1\rangle + \cos\left(\frac{\theta}{2}\right)|\psi_2\rangle. \tag{S88}$$

Taking the gradient yields

$$\nabla|\psi_-\rangle = -e^{-i\phi}\cos\left(\frac{\theta}{2}\right)\frac{d\theta}{2}|\psi_1\rangle + ie^{i\phi}\sin\left(\frac{\theta}{2}\right)d\phi|\psi_1\rangle + \sin\left(\frac{\theta}{2}\right)\frac{d\theta}{2}|\psi_2\rangle. \tag{S89}$$

Multiplying eq. (S89) by $\langle\psi_-|$ results in

$$\begin{aligned}\langle\psi_-|\nabla|\psi_-\rangle &= -\cos\left(\frac{\theta}{2}\right)\sin\left(\frac{\theta}{2}\right)\frac{d\theta}{2} + \sin\left(\frac{\theta}{2}\right)\cos\left(\frac{\theta}{2}\right)\frac{d\theta}{2} - i\sin^2\left(\frac{\theta}{2}\right)d\phi \\ &= -i\sin^2\left(\frac{\theta}{2}\right)d\phi = -\frac{i}{2}(1-\cos\theta)d\phi. \end{aligned} \tag{S90}$$

Thus, the Berry phase for the lower state is given by

$$\gamma_- = \int_0^{2\pi} i\langle\psi_-|\nabla|\psi_-\rangle d\phi = \pi(1-\cos\theta). \tag{S91}$$

Hence, in both cases, the integration range is defined by $d\phi$. In our scenario, the integration corresponds to dk_z in the Brillouin zone, where z defines the propagation axis of the seed pulse. Since the Brillouin zone can be mapped onto a circle (see Fig. 4 in the main text), the Berry phase of the Brillouin zone and the Bloch sphere should be equivalent:

$$\gamma_{\pm} = \oint A(k_z)dk_z = \int_0^{2\pi} A(\theta)d\phi. \tag{S92}$$

Thus, the S^1 topology of the one-dimensional Brillouin zone along the k_z-direction can be adiabatically mapped onto the polar angle ϕ of the Bloch sphere. However, a similar mapping also applies to the k_x- and k_y-directions, even without invoking an adiabatic process. In eq. (S62), we access the k_x-direction of the Brillouin zone at $t = 0$. Consequently, the S^1 topology naturally applies here as well, but now oriented perpendicular to the k_z-direction. Therefore, k_x at $t = 0$ can be mapped to $\tilde{z}$. Using the definition of $\tilde{z}$ in eq. (S83), we obtain

$$k_x a = 2\pi \cos\theta, \tag{S93}$$

where the factor of 2π arises from normalization. This relation follows from the one-point compactification (Alexandroff compactification) of $\mathbb{R}^2$, which yields the topological structure of the S^2 sphere as shown in Fig. S10. Substituting eq. (S93) into the fit function eq. (S62) and summing over the k-points in the z-direction, the resulting Berry phase exhibits the expected dependence as given by eqs. (S87) and (S91), as shown in Fig. 5 of the main text and Fig. S11 for $\lambda = 343\,\mathrm{nm}$ (orange curve) and $\lambda = 348\,\mathrm{nm}$ (blue curve). In both figures, the offset has been removed and the Berry phase is normalized to 2π. The Berry phase was determined by summing over the k_z-axis of Fig. S12 for the orange curve and Fig. S13 for the blue curve. The results justify the assumption to map the Bloch sphere onto the Brillouin zone

However, in order to fulfill this relation, the basis of the Landau-Zener effect has to change. That means that the tunnelling has to occur in k_x-

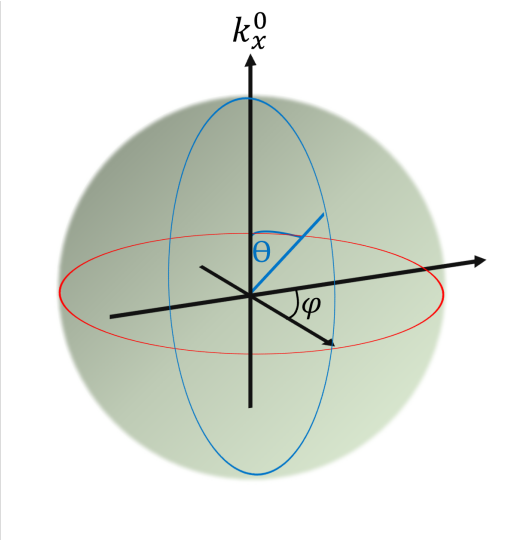

Figure S10: One-point compactification of the Brillouin zone. The φ component is adiabatically mapped as shown in the main text in Fig. 4c. For the k_x^0 direction the usual S^1-topology is used to create a circle. This was shon in Fig. 4b in the main text.

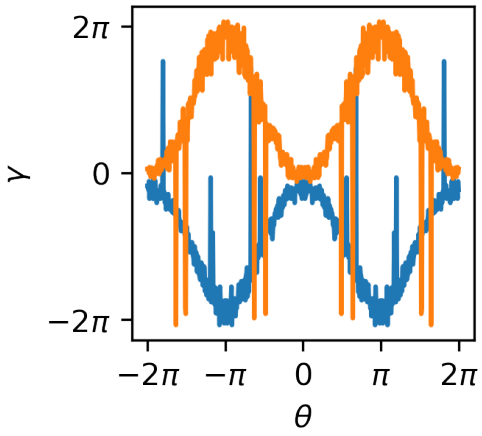

Figure S11: Extracted Berry phase γ as a function of θ, evaluated using eqs. (S93) and (S62), for the unmodulated (resonant) harmonic at $\lambda = 343\,\text{nm}$ (orange) and a modulated (non-resonant) harmonic at $\lambda = 348\,\text{nm}$ (blue). A comparison with the Berry phases of the entangled states $\psi_\pm$ from eqs. (S87) and (S91) reveals that the $\lambda = 343\,\text{nm}$ harmonic originates from the valence band associated with ψ_-, while the $\lambda = 348\,\text{nm}$ (and $\lambda = 335\,\text{nm}$) harmonics are generated in the conduction band described by ψ_+.

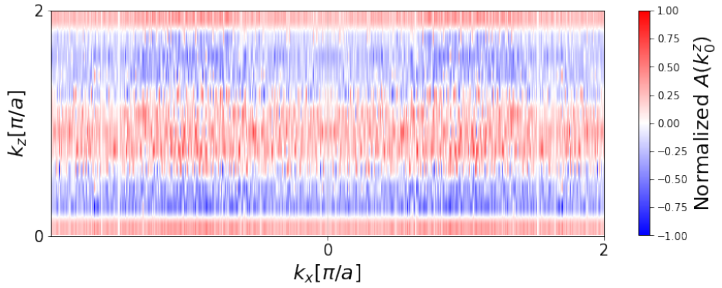

Figure S12: Dependence of the Berry connection as a function of $k_x a$ for the resonant harmonic $\lambda = 343\,\mathrm{nm}$.

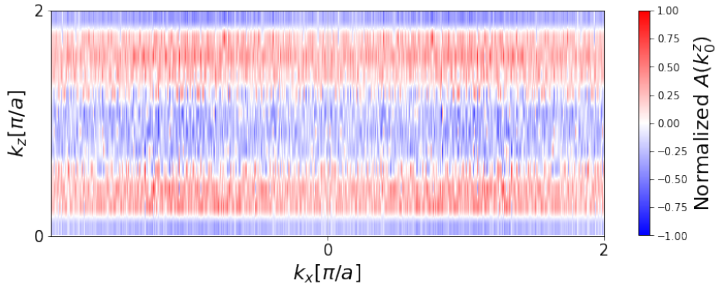

Figure S13: Dependence of the Berry connection as a function of $k_x a$ for the opto-magnetic harmonic $\lambda = 348\,\mathrm{nm}$.

direction. Thus the parameter Γ according to eq. (S79) changes to

$$\Gamma = \frac{E_g^2}{4v_k\hbar\frac{dk_x(t)}{dt}|_{t=0}} \tag{S94}$$

where $E_g = 8.9\,\mathrm{eV}$ is the band gap of quartz and $k_x(t)$ is the momentum of the electron parallel to the electric field according to eq. (S11). There it was denoted as $k_\parallel$.The time derivative of the momentum is given by

$$\frac{dk_x(t)}{dt}\Big|_{t=0} = -\frac{d}{dt}\frac{eE_0}{\hbar\omega_0}\sin(\omega_0 t)\Big|_{t=0} = -\frac{eE_0}{\hbar}\cos(\omega_0 t)\Big|_{t=0} = -\frac{eE_0}{\hbar} \tag{S95}$$

By using the Brillouin momentum $v_k = 2\pi\hbar/(m^* a)$ the transition probability according to eq. (S78) becomes the original Landau-Zener formula [18, 19]

$$P = \exp\left(-\frac{m^* a E_g^2}{4\hbar^2|eE_0|}\right). \tag{S96}$$

We note that the avoided crossing in this basis depends on the external field E_0 rather than time, as shown in the supplementary information of [15]. Consequently, the bandgap reduction due to Wannier-Stark localization, described by eq. (S66), is already incorporated in eq. (S96) and does not need to be included separately, as indicated in eq. (S82).

Fig. S14 displays the fit of eq. (S96) to the harmonic yield of the opto-magnetic modulated parts of the spectrum of the z-cut. Here, an effective mass of $m^* = 0.45 m_e$ for the $\lambda = 348\,\mathrm{nm}$ could be extracted. This matches the reported values of the electron effective mass in quartz reported before [20]. However this is significantly higher than the effective mass we extract from the Landau-Zener effect in k_z-direction. Here the lowering in effective mass is a consequence of the localized synchronization and the Wannier-Stark localization.

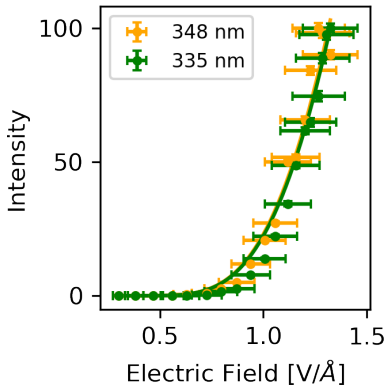

Figure S14: Fit of eq. (S96) to the harmonic yield of the opto-magnetic modulated parts of the spectrum of the z-cut.

14.1 Determination of the Berry Phases and Berry Connections using the Wannier-Stark Effective Mass

In eq. (S68), the effective mass was described as a function of the electric field and the constant length of a Wannier -Stark localization. An effective mass of $m^* \approx 0.04\, m_e$ was determined at a field strength of $1.4\,\mathrm{V/Å}$. It was assumed that the localization length is constant and given by the lattice constant $L_{\mathrm{WS}} = \Delta R = a$, where ΔR is defined in eq. (S44). This directly implies that the effective mass is not constant, but rather inversely proportional to the external electric field E_0. However, in Fig. S9, a constant effective mass was assumed. According to eq. (S67), this would imply a variable localization length L_{WS} that depends on the external field. Since the length also scales inversely with E_0 in this case, the localization would increase with increasing field strength. This leads to $L_{\mathrm{WS}} \neq \Delta R = a$ (in k_z-direction).
Given that different modelling approaches are now under consideration, their physical equivalence must be examined. Therefore, the Berry connection previously calculated in Fig. S9 under the assumption of a field-independent constant effective mass is re-calculated here using a field-dependent effective mass according to eq. (S68). To this end, eq. (S68) must be inserted into eq. (S62). Fig. S15 shows the corresponding Berry connection for the z-cut

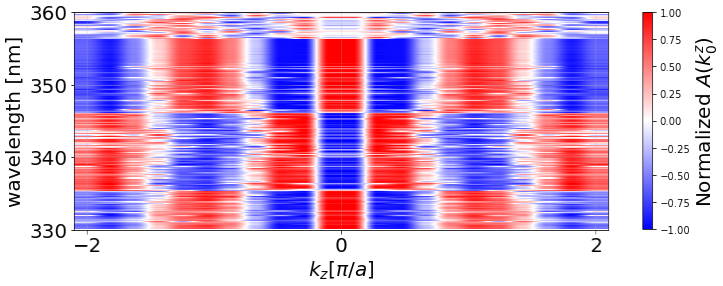

Figure S15: Normalized Berry connection for the z-cut using the field-dependent effective mass according to eq. (S68).

across all spectral components. The overall structure of the Berry connection as a function of the k_z direction is clearly preserved, with the opto-magnetically modulated components consistently maintaining their characteristic sign reversal. However, slight variations in the spectral width of the phase are noticeable.

For a more detailed analysis, a fixed point along the k_z direction is considered, namely $k_z = 0$. From Figure S15, it can be seen that the blue region lies within the spectral range between $\lambda = 337\,\mathrm{nm}$ and $\lambda = 345\,\mathrm{nm}$. The corresponding phase jump to the red region, which indicates the sign change in the Berry connection, occurs both below and above this interval. In contrast, Figure S9 shows the blue region at $k_z = 0$ within a slightly narrower range between $\lambda = 340\,\mathrm{nm}$ and $\lambda = 345\,\mathrm{nm}$. Additionally, in this representation the Berry connection is out of phase for wavelengths below $\lambda = 333\,\mathrm{nm}$. However, the central main maxima are in phase in both cases, in Fig. S9 and Fig. S15. This suggests that the fits differ primarily in the low-intensity spectral regions, whereas they agree in the vicinity of the main maxima, which are the spectrally relevant domains.

It remains to demonstrate the equivalence of the Berry phase. For this purpose, the substitution using eq. (S93) and eq. (S68) is again performed in eq. (S62), followed by integration along the k_z direction from 0 to 2π. Figure S16 shows the resulting Berry connection as a function of the Bloch angle θ for the spectral range around $\lambda = 334\,\mathrm{nm}$ (orange) and for the spectral range around $\lambda = 335\,\mathrm{nm}$ (blue). It is readily apparent that the structure described

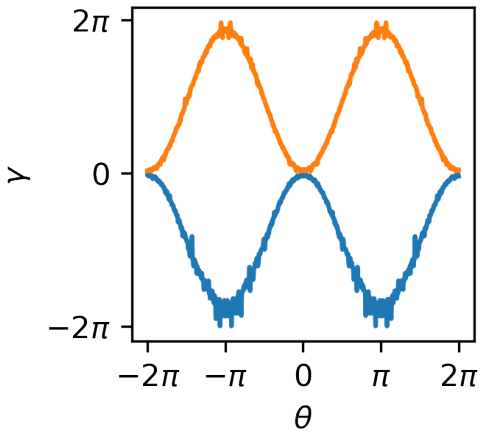

Figure S16: Berry phase γ for the z-cut as a function of the Bloch angle θ, obtained by integrating the Berry connection determined via eq. (S68) and eq. (S62). The blue curve corresponds to the spectral range around $\lambda = 335\,\text{nm}$, while the orange curve represents the resonant spectral range at $\lambda = 343\,\text{nm}$. The sampling rate of the Brillouin zone is $0.1\frac{\pi}{a}$.

by eq. (S87) and eq. (S91) is preserved. The resulting Berry phases, shown in Fig. 5f in the main text and Fig. S11, differ only by numerical noise. As in the aforementioned figures, the background was subtracted in Figure S16, and the Berry phases for both spectral regions — and thus for both energy bands described by the pseudo-spin vectors — were normalized to 2π. The final remaining aspect of the spectral analysis is to verify the sampling in k-space.

14.2 Determination of the Berry Phase and Berry Connection with symmetrical integration limits

In the previous three sections, the equivalence of three different methods for extracting the formal Berry phase as a function of the Bloch angle from the spectral data has been demonstrated. These methods involved comparing different samplings of the Brillouin zone under the assumption of a constant effective electron mass in the k_z-direction. Although the Berry connections

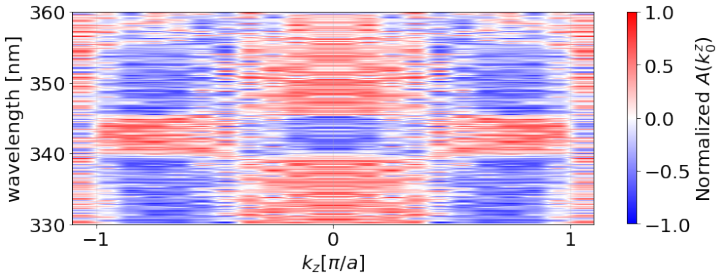

Figure S17: Berry connection obtained from the spectrum generated for the z-cut using a constant effective mass and a sampling rate of $0.1\,\pi/a$ and symmetrical integration limits $[-\pi/a, \pi/a]$. The sign reversal of the opto-magnetically modulated and resonant spectral components is preserved, although the Berry connection differs formally from that shown in Fig. S9.

differ between the approaches, integration over k_z yields Berry phases for the upper and lower states ψ_+ and ψ_- that remain consistent with the functional forms given in eq. (S87) and eq. (S91). Assuming a constant effective mass implies a variable length of the Wannier- Stark states as a function of the electric field E_0, according to eq. (S67). Conversely, if the length of the Wannier- Stark states is fixed, i.e., $L_{\mathrm{WS}} = \Delta R = a$, the effective mass becomes field-dependent. The equivalence of the resulting Berry connection for the z-cut has been demonstrated in Fig. S9 for the case of constant effective mass (implying a field-dependent localization length), and in Fig. S15 for the case of a variable effective mass with fixed localization length.
The final method to be validated concerns the integration limits. This analysis is performed under the assumption of a constant effective mass. Figure S17 shows the resulting Berry connection for the z-cut at the with symmetrical integration limits ($k_z \in [-\pi/a, \pi/a]$). It is immediately evident that the Berry connection formally differs from that shown in Fig. S9.

However, the characteristic sign change in the Berry connection around the resonant and opto-magnetically modulated spectral regions remains clearly visible.
It remains to be verified whether the substitution according to eq. (S93), followed by integration over the k_z-direction, still yields the Berry phase of the entangled states as given by eq. (S87) and eq. (S91). This is indeed

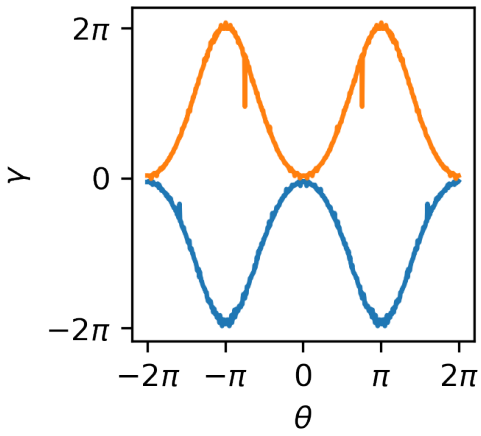

Figure S18: Extracted Berry phase γ for the z-cut as a function of the Bloch angle θ, shown for the spectral components at $\lambda = 343\,\mathrm{nm}$ (orange) and $\lambda = 348\,\mathrm{nm}$ (light blue), using a reduced Brillouin zone sampling rate of $0.1\,\pi/a$ and symmetrical integration limits $[-\pi/a, \pi/a]$.

the case. Figure S18 shows the resulting Berry phases. The method remains unchanged: in both cases, the background is removed, and the curves are subsequently normalized to 2π. The $(1 - \cos(\theta))$-dependence of the Berry connection, as described by eq. (S87) and eq. (S91) for the two entangled states characterized by the pseudo-spin vectors in eq. (S72) and eq. (S73), is preserved. It is particularly noteworthy that the resulting Berry phase for these two states no longer exhibits numerical noise. The numerical noise observed previously is thus identified as an artifact of the fitting procedure, and can be considered entirely unphysical and safely disregarded.

In summary, the spectra have been analyzed using four different methods. While the Berry connection formally differs in all four approaches—as expected—the resulting Berry phase consistently exhibits the characteristic $(1 - \cos(\theta))$ dependence of the entangled states. Consequently, the method that is numerically the most straightforward and yields the most reliable results may be confidently applied.

References

1. El-Sayed, A.-M., Tanimura, K. & Shluger, A. Optical signatures of intrinsic electron localization in amorphous SiO2. *Journal of Physics: Condensed Matter* **27,** 265501 (2015).
2. Sushko, P. V., Mukhopadhyay, S., Stoneham, A. M. & Shluger, A. L. Oxygen vacancies in amorphous silica: structure and distribution of properties. *Microelectron. Eng.* **80,** 292–295 (2005).
3. Bloch, F. Über die Quantenmechanik der Elektronen in Kristallgittern. *Zeitschrift für Physik* **52,** 555–600 (1929).
4. Kramers, H. A. Théorie générale de la rotation paramagnétique dans les cristaux. *Proceedings of the Royal Netherlands Academy of Arts and Sciences* **33,** 959–972 (1930).
5. Luu, T. T. & Wörner, H. J. Measurement of the Berry curvature of solids using high-harmonic spectroscopy. *Nat. Commun.* **9,** 916 (2018).
6. Liu, H. *et al.* High-harmonic generation from an atomically thin semiconductor. *Nature Phys.* **13,** 262–26 (2017).
7. Butcher, P. N. & Cotter, D. *The Elements of Nonlinear Optics* (Cambridge University Press, 1990).
8. Ghimire, S. & Reis, D. A. High-harmonic generation from solids. *Nature Phys.* **15,** 10–16 (2019).
9. Uzan-Narovlansky, A. J. *et al.* Observation of interband Berry phase in laser-driven crystals. *Nature* **626,** 66–71 (2024).
10. Lu, I.-T., Park, J., Zhou, J.-J. & Bernardi, M. Ab initio electron-defect interactions using Wannier functions. *npj. Comput. Mater.* **6,** 17 (2020).
11. Marzari, N., Mostofi, A. A., Yates, J. R., Souza, I. & Vanderbilt, D. Maximally localized Wannier functions: Theory and applications. *Rev. Mod. Phys.* **84,** 1419–1475 (2012).
12. Resta, R. & Vanderbilt, D. in *Physics of ferroelectrics: a modern perspective* 31–68 (Springer, 2007).

13. Kim, D., Shin, D., Landsman, A. S., Kim, D. E. & Chacón, A. Theory for all-optical responses in topological materials: The velocity gauge picture. *Phys. Rev. B* **106,** 214314 (2022).

14. Wang, Y., Zhu, Z.-G. & Su, G. Field-induced Berry connection and anomalous planar Hall effect in tilted Weyl semimetals. *Phys. Rev. Res.* **5,** 043156 (2023).

15. Schiffrin, A. *et al.* Optical-field-induced current in dielectrics. *Nature* **493,** 70–74 (2013).

16. Lakhotia, H. *et al.* Laser picoscopy of valence electrons in solids. *Nature* **583,** 55–59 (2020).

17. Uzan-Narovlanskya, A. J. *et al.* Observation of light-driven band structure via multiband high-harmonic spectroscopy. *Nat. Photon.* **16,** 428–432 (2022).

18. Landau, L. D. Zur Theorie der Energieübertragung. II. *Physics of the Soviet Union* **2,** 36–51 (1932).

19. Zener, C. Non-adiabatic crossing of energy levels. *Proc. R. Soc. Lond. A* **136,** 696–702 (1932).

20. Lenzlinger, M. & Snow, E. Fowler-Nordheim tunneling into thermally grown SiO2. *Journal of Applied physics* **40,** 278–283 (1969).